

High-pressure structural investigation on lead-free piezoelectric $0.5Ba(Ti_{0.8}Zr_{0.2})O_3 - 0.5(Ba_{0.7}Ca_{0.3})TiO_3$

Anshuman Mondal¹ | Pinku Saha¹ | Bishnupada Ghosh¹ | Mrinmay Sahu¹ |
Goutam Dev Mukherjee¹  | Rajeev Ranjan² | Kumar Brajesh³

¹Department of Physical Sciences, Indian Institute of Science Education and Research Kolkata, Nadia, India

²Department of Materials Engineering, Indian Institute of Science, Bengaluru, India

³Department of Material science and Engineering, Indian Institute of Technology Kanpur, Kanpur, India

Correspondence

Goutam Dev Mukherjee, Department of Physical Sciences, Indian Institute of Science Education and Research Kolkata, Mohanpur 741246, Nadia, West Bengal, India.

Email: goutamdev@iiserkol.ac.in

Funding information

Department of Science and Technology, Govt of India; Ministry of Earth Sciences, Grant/Award Number: MoES/16/25/10-RDEAS

Abstract

The solid solution $0.5Ba(Ti_{0.8}Zr_{0.2})O_3 - 0.5(Ba_{0.7}Ca_{0.3})TiO_3$ (BCZT) has become a promising member of the lead-free piezoelectric materials because of its exceptionally high piezoelectric properties. In this study, we focus on studying pressure-dependent Raman spectroscopy, powder x-ray diffraction, and dielectric constant measurements on BCZT. The data show several structural transitions are present, where the system from ambient mixed phase (tetragonal $P4mm$ + orthorhombic $Amm2$) transforms into single phase ($P4mm$) at 0.3 GPa, then converts into cubic phase ($Pm3m$) at 4.8 GPa followed by another possible structural re-ordering around 10 GPa. Although there have been a lot of unanimity with the ambient crystallographic state of BCZT, our analysis justifies the presence of an intermediate orthorhombic phase in the Morphological Phase Boundary (MPB) of BCZT phase diagram. The transformation tetragonal to cubic is indicated by the Raman mode softening, unit cell volume change, and the $(Ti/Zr)O_6$ octahedra distortion, which coincides with the well-known ferroelectric-paraelectric transition of the system. The sudden drop in the dielectric constant value at 4.7 GPa also confirms the loss of ferroelectric nature of the BCZT ceramic.

1 | INTRODUCTION

During last few decades, to avoid the hazardous effects of lead (Pb), there have been ongoing efforts to replace the commercially used lead-zirconate-titanate (PZT)-based piezoelectric materials with the lead-free materials having high piezo-response.¹⁻⁵ Among them, $0.5Ba(Ti_{0.8}Zr_{0.2})O_3 - 0.5(Ba_{0.7}Ca_{0.3})TiO_3$ (BCZT) has drawn significant attention because of its very high piezoelectric properties (~ 600 pC/N)^{6,7} in comparison with that of PZT (500-600 pC/N). The main reason lies within the phase diagram of solid solution BCZT having a Morphological Phase Boundary (MPB) that includes a triple point at the inter-section of paraelectric cubic, ferroelectric rhombohedral and tetragonal phases.⁶ Also it is reported that the piezoelectric properties are maximized at the tetragonal-rhombohedral phase

boundary.⁶ But there has been an ongoing debate on the crystallographic state of the BCZT composition at ambient conditions. Studies by Keeble et al⁸ and Tian et al⁹ have proposed that there exists an intermediate orthorhombic (O) phase in between rhombohedral(R) and tetragonal (T) phases making the "polarization rotation" possible between the two crystallographic groups. Furthermore, experimental studies by Zhang et al¹⁰ and Acosta et al¹¹ confirm that instead of the MPB (T-R phase boundary), the T-O phase boundary is responsible for the large piezo-response of the BCZT ceramics. It is also shown that a mere 2% of Zr, Sn, or Hf substitution in parent $BaTiO_3$ can stabilize a co-existence of orthorhombic and tetragonal phases at room temperature.¹² Although the presence of this orthorhombic phase is countered and also argued as an anomaly that arises due to the adaptive diffraction of tetragonal/

rhombohedral nanodomains.¹³⁻¹⁶ Brajesh et al^{17,18} have performed careful structural and dielectric studies on BCZT and concluded in favor of three-phase co-existing model (P4mm + Amm2 + R3m) to explain its giant piezo-response and relaxor ferroelectric nature. But it may give rise to a scenario of violating Gibb's phase rule if the orthorhombic phase is present all the way up to the critical point of the phase diagram. The study by Yang et al¹⁹ explains the largest piezoelectricity as well as the largest elastic softening of BCZT at the T-O phase boundary by the systematic energy barrier (EB) calculations that measures the degree of polarization anisotropy. So, one needs careful investigation on the ambient crystallographic state of the BCZT ceramic.

BCZT is one of the most well-studied systems. Microstructure basis for strong piezoelectricity in BCZT via transmission electron microscopy (TEM) is shown by Gao et al.¹³ Fan et al have carried out an in situ TEM study using unipolar electric field and shown that ferroelectric domains are disrupted by defect states.²⁰ The effect of grain size on the electrical properties and temperature dependence of variation in dielectric constant are shown by Hao et al.²¹ Temperature induced anomalies in the dielectric, piezoelectric, and elastic coefficients and Raman spectroscopy of ceramic BCZT are reported by Damjanovic et al.⁷ Piezoelectric property measurements by Piezo-response Force Microscopy (PFM) mode of Scanning probe microscopy (SPM) technique is reported by Coondoo et al,³ whereas piezo-properties on pulsed laser-deposited thin films are reported by Piorra et al.²² Based on all these available literature, it can be concluded that the piezoelectric properties of lead-free BCZT system is comparable to the PZT. But after the Curie temperature (T_c) at 97°C, all studies have shown a drop in the temperature-dependent dielectric constant values and have concluded this to loss of ferroelectric nature of the sample following a phase transition into cubic phase. Curie temperature (T_c) is found to vary by grain size changing²¹ or even by doping.^{12,23-26}

Although there are several temperature-dependent studies,^{3,7,9,10,21} to the best of our knowledge, BCZT certainly lacks the pressure-dependent measurements. Pressure is an important thermodynamic variable that can tune the inter-atomic distance precisely changing the free energy of the system. The volume compression can lead to change in internal strain giving rise to several changes in the physical properties of the material leading to novel phase transitions that may include structural, electronic transitions etc.²⁷⁻²⁹ BCZT, which is a solid solution of BZT-BCT, hold all the properties of its parent material BaTiO₃ along with the effect of doping on it. Therefore, the present manuscript focuses on high-pressure Raman spectroscopy, x-ray diffraction, and dielectric measurements of BCZT to study

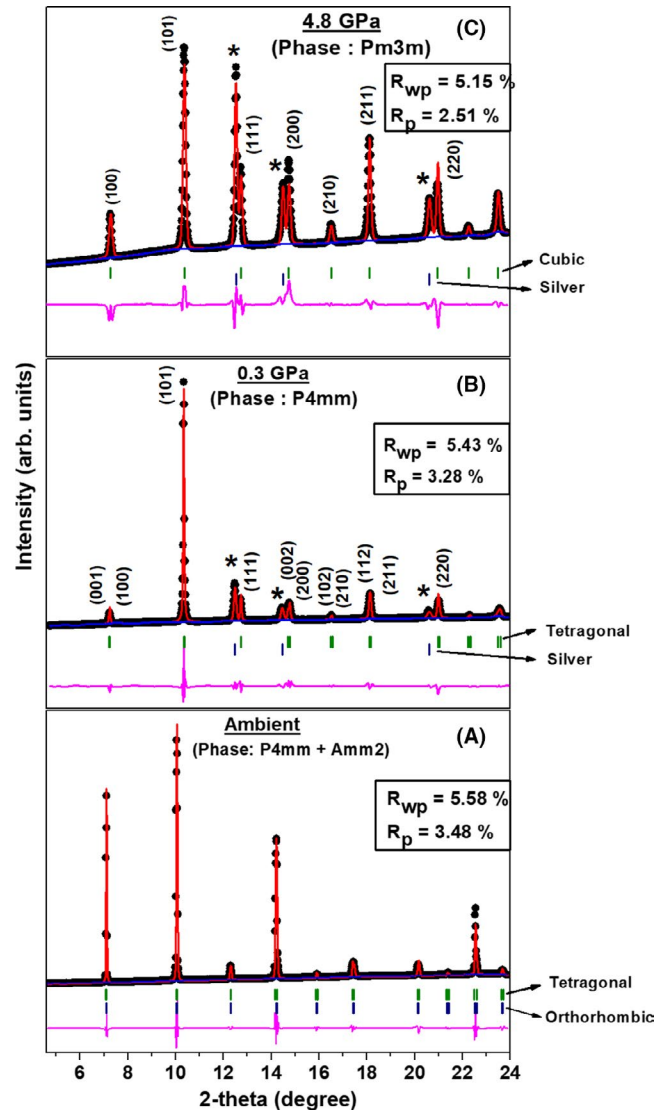


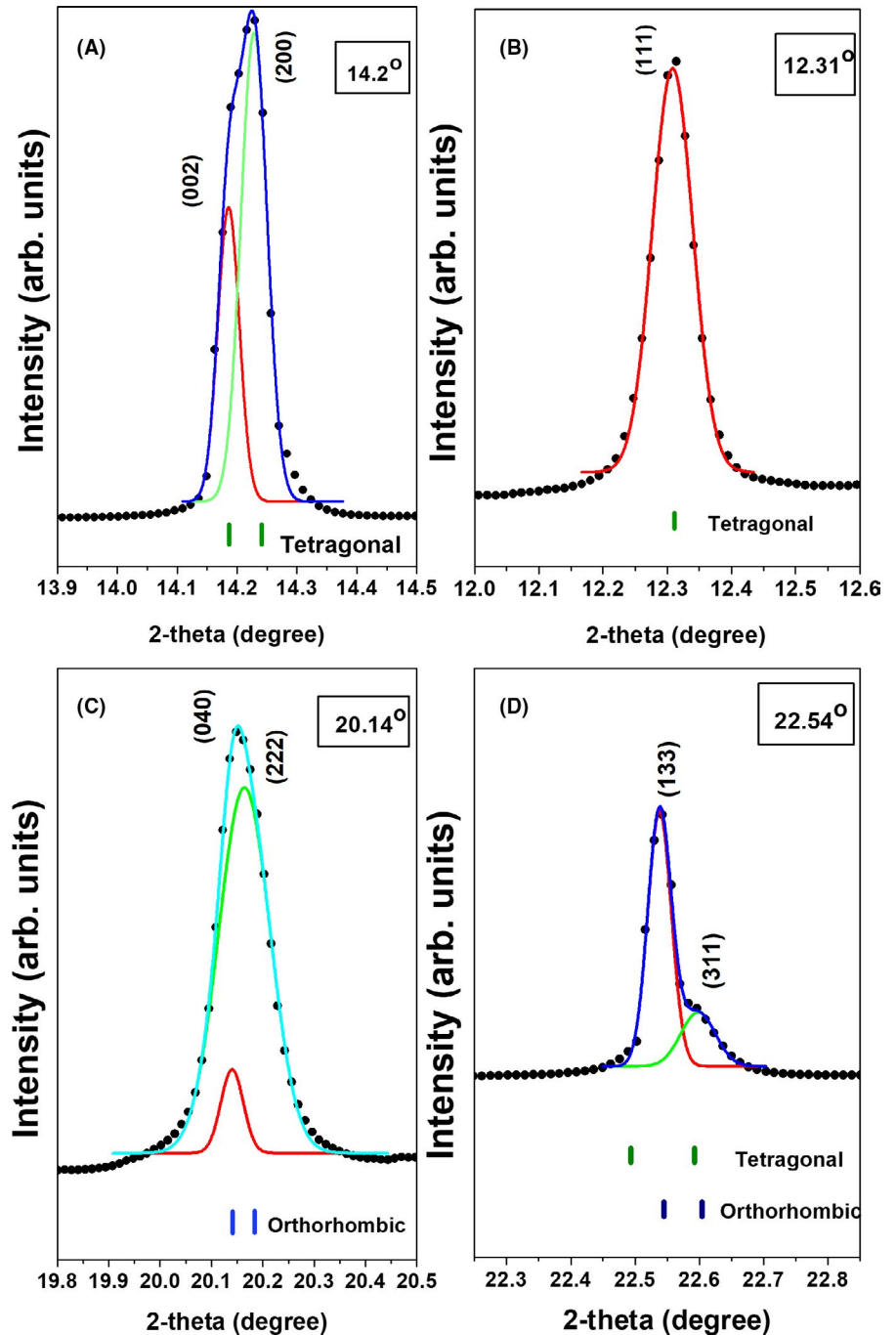
FIGURE 1 HYPERLINK "sps:id::fig1|locator::gr1" Rietveld refinement of BCZT XRD patterns at (A) ambient pressure (with mixed phase tetragonal and orthorhombic), (B) 0.3 GPa (with only tetragonal phase), and (C) 4.8 GPa (with cubic phase). Black dots represent the data points, red line is the fitted line, and pink line below represents the difference between the observed and the fitted intensities. "*" indicates the pressure-marker Silver (Ag). The goodness of fit parameters (R_{wp} and R_p) are given in the boxes

phase transitions, which modify its dielectric properties and piezoelectric nature.

2 | EXPERIMENT

Polycrystalline powder sample 0.5Ba(Ti_{0.8}Zr_{0.2})O₃ - 0.5(Ba_{0.7}Ca_{0.3})TiO₃ (or BCZT) is prepared via conventional solid-state reaction method.¹⁷ High-pressure x-ray diffraction (XRD) and Raman spectroscopic measurements are performed using diamond-anvil cell (DAC)

FIGURE 2 Fitting of Bragg peaks implying tetragonal and orthorhombic nature of ambient BCZT. A, Doublet nature of 14.2° peak and (B) singlet nature of 12.31° peak imply the structure to be tetragonal. C, The doublet nature of 20.14° peak and (D) the 22.54° peak is fitted best with the orthorhombic phase imply the presence of orthorhombic phase too



from EasyLab Co. (UK) with a culet size of $300\ \mu\text{m}$. To hold the sample in between two opposing diamonds, a pre-indented metal gasket (indented thickness $\sim 50\ \mu\text{m}$) is used with a $100\ \mu\text{m}$ see-through hole at the centre of indentation. Methanol-ethanol mixture (4:1) is used as the pressure-transmitting medium (PTM) to maintain the hydrostatic condition. For the Raman-spectroscopic measurements, Monovista CRS + spectrometer is used along with an infinitely corrected long-working distance 20X objective. Pressure is determined by observing the shift of ruby fluorescence peak with ruby grains loaded alongside the sample inside DAC.³⁰ Sample is excited using a 532 nm

green laser and spectra are collected using a grating of 1500 grooves/mm in the back-scattering geometry with resolution of $1.2\ \text{cm}^{-1}$.

High-pressure XRD measurements are performed at the XPRESS beamline in the Elettra Synchrotron Source, Italy using a monochromatic wavelength of $0.4957\ \text{\AA}$. For XRD, a small amount of Ag powder is mixed along with the sample and pressure is calculated using the well-known Birch-Murnaghan equation of state of Ag.³¹ The incident x-ray is collimated to $30\ \mu\text{m}$ and a MAR-3450 image plate detector is used to detect the diffracted x-rays, aligned normal to the beam. The sample to detector distance is calibrated using

LaB₆ and all the diffracted patterns are integrated to intensity vs 2 θ profiles using FIT2D software³² and then further analyzed using CRYSFIRE³³ and GSAS.³⁴

High-pressure dielectric constant measurements are carried out up to 5.5 GPa using the large-volume Toroid-anvil (TA) cell and a 300-ton hydraulic press. The TA apparatus is calibrated using Bi I-II and Yb hcp-bcc transitions at 2.65 GPa and 4 GPa, respectively.³⁵ The sample assembly is prepared and the frequency-dependent capacitance is measured as described by Jana et al.²⁷ The dielectric constant (K) is calculated using the expression, $C = K\epsilon_0(A/d)$, where ϵ_0 is the permittivity of the free space, C is the capacitance, A is the area of the copper plate, and d is the thickness of the sample pellet.

3 | RESULTS AND DISCUSSIONS

BCZT can be thought as Ca and Zr doping of the parent sample BaTiO₃, making a solid solution out of it. The sample is characterized by XRD measurements. Figure 1A shows the ambient XRD pattern. Indexing of the sample at ambient condition leads to a mixed phase of tetragonal and orthorhombic crystal structures supporting earlier reports.^{12,19} Using the initial atom positions given by Brajesh et al¹⁷ for the two phases, full structural Rietveld refinement has been carried out using the GSAS³⁴ software. In this refinement process, only the atom positions corresponding to Ti/Zr atom are refined and oxygen being a lighter atom is exempted from this refinement process.¹⁸ The lattice parameters obtained from the best-fit are—(i) for tetragonal phase: $a = 3.99906(9)$ Å, $c = 4.0208(1)$ Å, $\text{vol} = 64.303(3)$ Å³ and (ii) for orthorhombic phase: $a = 3.9980(1)$ Å, $b = 5.6775(2)$ Å, $c = 5.6670(1)$ Å, $\text{vol} = 128.635(7)$ Å³. In Figure 2, the singlet nature of the $2\theta = 12.31^\circ$ peak (111) and the doublet nature of the peak around $2\theta = 14.2^\circ$ [(002)/(200)] in the ambient XRD pattern are implying a tetragonal (P4mm) global structure.¹⁸ The asymmetric doublet nature of the peak around $2\theta = 20.14^\circ$ [(040)/(222)] in Figure 2C and the peak at $2\theta = 22.54^\circ$ [(133)/(311)] (Figure 2D), which can only be fitted with the orthorhombic phase, indicate the perovskite structure to be orthorhombic in nature too. With these two phases, we have an excellent fit that certainly sets aside the question of any anomaly that may have come due to the adaptive diffraction by the P4mm-R3m nanodomains as reported by Gao et al¹⁴ earlier. At ambient conditions, the presence of both the tetragonal and the orthorhombic phases are justified.

Ambient and high-pressure Raman spectroscopy measurements are performed on BCZT to explore the microscopic changes that occur due to the volume compression. Pressure evolution of Raman spectra at selected pressure points including the ambient pattern are shown in Figure 3A.

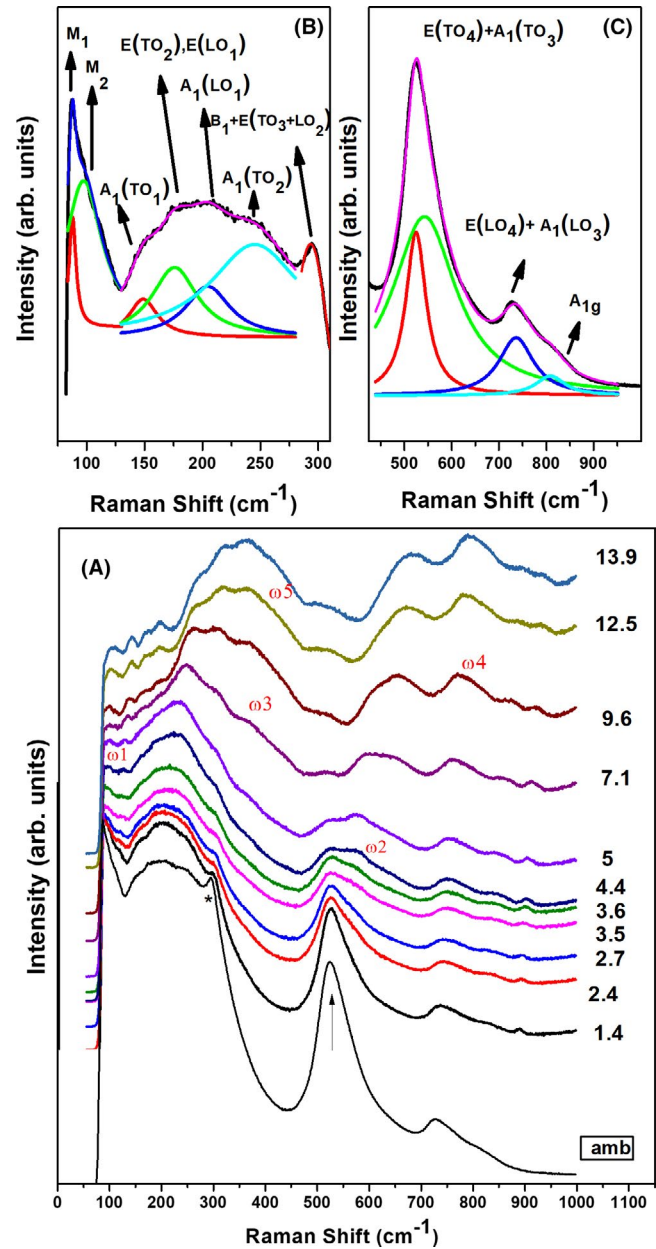


FIGURE 3 A, Evolution of Raman spectra starting from ambient (bottom) up to 13.9 GPa (top) at selected pressure values. The arrow indicates the E(TO₄)+A₁(TO₃) mode which softens and reduces its intensity rapidly with pressure and a second peak appears from its asymmetric tail above 3.5 GPa. The sharp nature of the "*" peak also reduces. With pressure softening of modes, line-shape change in low-frequency range and appearance of several new peaks (ω_1 , ω_2 , ω_3 , ω_4 , and ω_5 respectively) indicate structural rearrangement. B and C, De-convolution of BCZT ambient Raman spectra in the range 80-340 cm⁻¹ and 400-1000 cm⁻¹, respectively

The pattern shows broad Raman modes and looks similar to that of parent BaTiO₃.³⁶ Broad Raman modes indicate to the internal disorder of the system that arises due to the substitution in the unit cell of polycrystalline BaTiO₃.³⁷ Since theoretical Raman modes for BCZT are unavailable due to the

structural complexity, we indexed the ambient Raman spectrum following BaTiO₃ Raman mode assignments^{36,38-41} and also taking reference from earlier works.^{37,42} To determine the Raman mode frequency positions, we have performed the Lorentz fitting of each peak shown in Figure 3B,C. The most important feature of this kind of systems is the presence of several anharmonic modes in the low-frequency range. The dip at 130 cm⁻¹ is referred as anharmonic coupling mode that comes due to the interference between the three A₁(TO) modes³⁶. All the modes with their corresponding frequency positions are listed in Table 1. It can be seen that some Raman peaks are assigned to multiple phonon modes as frequency position of a few A₁ and E modes are very close to each other and also the randomly oriented grains in a polycrystalline sample do not permit polarization selection between A₁ and E modes.^{36,37} We also have observed two new peaks M₁ (88 cm⁻¹) and M₂ (97 cm⁻¹), which could not be identified with BaTiO₃ modes. The low-frequency modes are due to vibration of heavy atoms. Therefore, these extra peaks can be related to the substitution of Ca and/or Zr ions and the defects that might have occurred due to these substitutions. The low-frequency shift of the A₁(TO₁) and A₁(TO₂) modes compared to parent BaTiO₃ mode frequency positions can be related to the Ca substitution in the system.^{37,41} Blue shift of peaks to higher frequency for the 525 cm⁻¹ and 737 cm⁻¹ modes are expected due to the different ionic radius of Ba⁺²/Ca⁺² and Ti⁺⁴/Zr⁺⁴ that induces distortion in the lattice resulting energy band widening.⁴² The peak at 525 cm⁻¹ corresponds to the TiO₆/ZrO₆ octahedral deformation mode. The asymmetric nature of this mode can be attributed to the combination of normal E(TO₄)+A₁(TO₃) mode along with modes arising due to defects in the system.⁴³ In addition to this, a feeble mode is observed at 809 cm⁻¹ which is not present for parent BaTiO₃. It can be referred as octahedral

breathing mode (A_{1g}), that become Raman active for the presence of several dissimilar ions in the complex perovskite solid solution.^{37,42}

It can be seen from Figure 3A that with pressure, the dip around 130 cm⁻¹ reduces, and similar observation has also been found by Basu et al.²⁸ The reason behind this can be the increase in anharmonic contributions of all the low-frequency modes that is evident from Figure 3A. However, all the modes broaden and their frequencies increase with pressure, anomalous behavior is observed for A₁(TO₂) mode at 245 cm⁻¹ and E(TO₄) + A₁(TO₃) mode at 525 cm⁻¹. The A₁(TO₂) mode softens with increase in pressure up to 5.3 GPa, then starts increasing (see Figure 4). E(TO₄)+A(TO₃) mode also softens with a slope change above 5 GPa. The high-frequency modes can be related to light atom vibrations such as, Ti-O/Zr-O bond vibrations. Therefore, this anomalous behavior of E(TO₄)+A(TO₃) mode is certainly due to the (Ti/Zr)O₆ octahedral distortion in the system that tends to gain more symmetry with applied pressure. The sharp kink at 293 cm⁻¹ loses its sharp nature beyond 4.4 GPa. The asymmetric peak around 525 cm⁻¹ loses its intensity with pressure and shows a second peak on its asymmetric tail (Figure 3A) for pressures above 3.5 GPa. Above 4.4 GPa, the new peak tends to increase, exceeding the old one in intensity. The pressure induced modification leads to the loss of the A₁(LO₁) mode beyond 4.4 GPa. Two new modes observed from 4.4 GPa onwards at 124 cm⁻¹ and 632 cm⁻¹ are referred as ω₁ and ω₂, respectively (see Figure 3A). In the low-frequency range, appearance of new modes can be related to heavy atom (Ba/Ca) vibrations.²⁸ Softening of low-frequency Raman modes are associated with decrease in polarization in the sample leading to change in ferroelectric nature.³⁶ Softening of modes, appearance of two new modes (ω₁ and ω₂), disappearance of A₁(LO₁) mode, loss of sharp nature of the peak at 293 cm⁻¹,

TABLE 1 Ambient Raman mode frequency values of BCZT

Mode symmetry	BCZT observed mode frequency (cm ⁻¹)	BaTiO ₃ mode frequency (cm ⁻¹) ³⁸	References
M ₁	88	Absent	
M ₂	97	Absent	
A ₁ (TO ₁)	149	178	[37,42]
E(TO ₂), E(LO ₁)	176	180	[38,39]
A ₁ (LO ₁)	205	189	[37,38]
A ₁ (TO ₂)	245	267	[36,38,40,9]
E(TO ₃ + LO ₂) + B ₁	293	308	[36,37]
E(TO ₄)	525	489	[36,39,40,42]
A ₁ (TO ₃)	525	512	[36,39,40,42]
E(LO ₄)	737	722	[37,42]
A ₁ (LO ₃)	737	740	[37,42]
A _{1g}	809	Absent	[37,42]

Note: The observed Raman mode frequencies are compared with BaTiO₃.

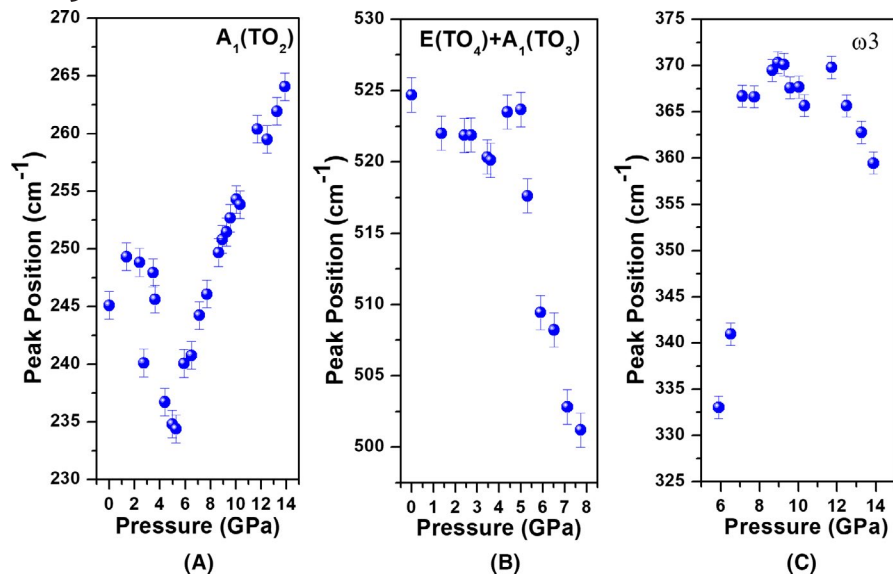


FIGURE 4 Evolution of $A_1(\text{TO}_2)$, $E(\text{TO}_4)+A_1(\text{TO}_3)$ and ω_3 modes with pressure. A, $A_1(\text{TO}_2)$ mode initially softens up to 5.3 GPa, then increases with further increase in pressure. B, $E(\text{TO}_4)+A_1(\text{TO}_3)$ mode shows an overall softening kind of nature with pressure up to 8 GPa with a slope change at about 5 GPa. C, The frequency position of the new peak ω_3 initially increases, followed by a large drop above about 11 GPa implying structural re-ordering

and decrease in intensity of the 525 cm^{-1} mode are the characteristics of change in crystal structure. The weak peak near 886 cm^{-1} can be seen throughout all pressure plots except the ambient spectra. The position of this mode changes at very high rate ($3.3 \text{ cm}^{-1}/\text{GPa}$) and can be related to the C-C stretching of ethanol-methanol pressure transmitting medium. Beyond 5 GPa, with increase in pressure we have observed several other additional interesting features. It includes the loss of $E(\text{TO}_4) + A_1(\text{TO}_3)$ mode at 10.3 GPa and several new peaks appear at 333 cm^{-1} (ω_3), 809 cm^{-1} (ω_4) and 418 cm^{-1} (ω_5) from 5.9, 9.6 and 12.5 GPa pressure points, respectively (see Figure 3A). With pressure, the frequency of all these new modes increases up to the highest pressure point of our study. The ω_3 mode initially increases up to about 11.7 GPa followed by a sharp drop (Figure 4). Softening of certain Raman modes and appearance of several new modes indicate to certain structural re-ordering. Softening of $A_1(\text{TO}_2)$ and $E(\text{TO}_4)+A_1(\text{TO}_3)$ modes indicate to loss of ferroelectricity. Therefore, the application of pressure pushes the system into a more symmetric paraelectric phase. The presence of Raman spectra beyond this transition in the paraelectric phase can be explained by order-disorder model in which the Ti/Zr atoms are not sitting in the exact body-centered position of the octahedra. It is slightly distorted along the body diagonal which breaks the inversion symmetry allowing the Raman activity.^{36,37,44} However, direct structural determination is not possible using Raman spectroscopy; but it is more likely to present the instantaneous changes in atomic positions. X-ray diffraction studies are required for further understanding.

To observe a direct change in the ferroelectric properties of BCZT, we have performed high-pressure dielectric constant measurements. Figure 5A shows the variation in dielectric constant (ϵ) and dielectric loss (δ) values from 0.35 GPa to up to 5.41 GPa for some selected frequency values (50 Hz, 100 Hz, 500 Hz, 1 KHz, 5 KHz, 10 KHz, 50 KHz,

100 KHz, 500 KHz, 1 MHz). At each frequency, 10 consecutive measurements of capacitance and loss are taken and the mean value is determined. The value of the dielectric constant at 0.35 GPa is matching with the reported result.⁴⁵ At all pressure points, ϵ shows an exponential-like decrease with frequency. In addition, at a constant frequency (mainly at low frequency) ϵ value decreases with increase in pressure and above 4.69 GPa it seems to saturate. Now, if we observe the dielectric constant value at 0.8 GPa at 50 Hz frequency (shown in Figure 5A), it is around 1875. In comparison at ambient conditions the dielectric constant value has been found to be 3085 for a large pellet of BZT¹⁶ at 100 Hz, which of the same order of magnitude. Such a large value of dielectric constant can come from both the contribution of intrinsic and extrinsic factors. These extrinsic factors include contributions due to the Maxwell-Wagner effect and also the effect of grain boundaries in such a polycrystalline system. To properly understand this, we have plotted the variation of dielectric constant and dielectric loss value with frequency at 6.82 GPa pressure (see Figure 5B). Here the dielectric constant shows a drop and this drop matches with the peak of dielectric loss in between 500 and 1000 Hz indicating a Debye-like relaxor behavior arising due to the Maxwell-Wagner effect.²⁹ Strong frequency dependence in dielectric constant can be modeled in terms of an equivalent circuit consisting of two parallel R-C circuits connected in series, where one of the capacitance comes from the extrinsic effects and another corresponds to bulk intrinsic effects.²⁹ At high frequencies, above the peak frequency of the dielectric loss, the capacitance arising due to extrinsic effects get shorted, and intrinsic bulk behavior is observed. Therefore to study the pressure evolution of dielectric constant (see in Figure 5C), we have considered the 100 KHz frequency, that is, a high-frequency range data. In Figure 5C, we have shown the pressure dependence of dielectric constant ϵ and

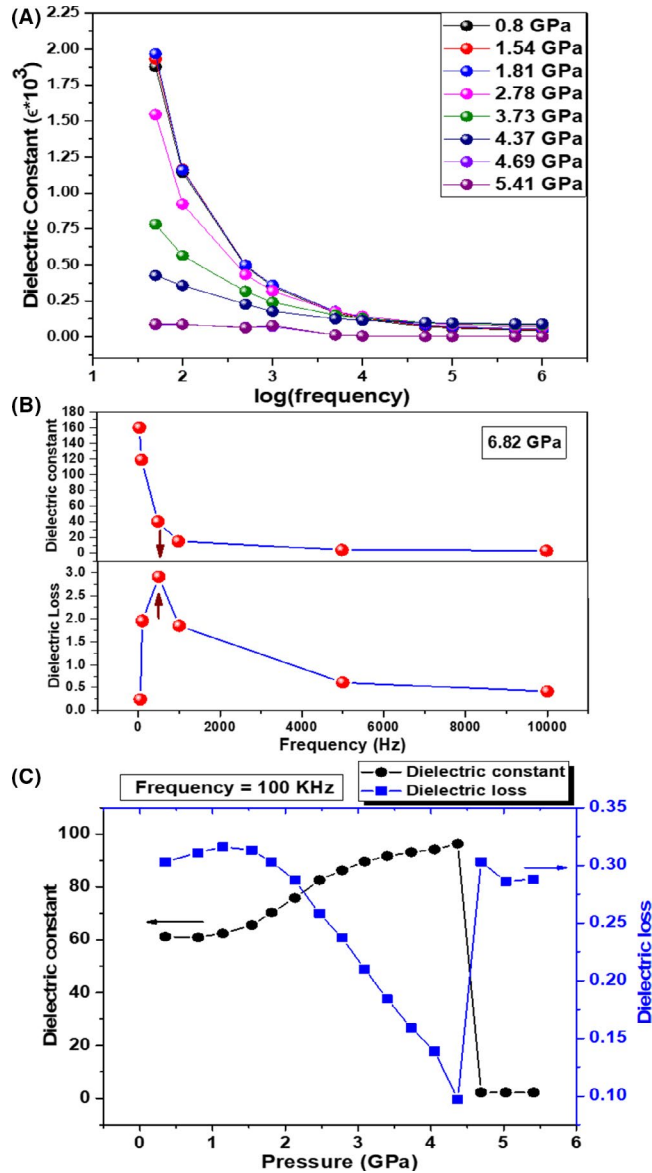


FIGURE 5 A, Frequency dependence of the dielectric constant value of BCZT at selected pressures showing exponential like decreasing nature. B, Frequency dependence of dielectric constant and loss at 6.82 GPa pressure showing Debye-like relaxation behavior at high frequencies. C, Pressure dependence of dielectric constant ϵ (shown in dots) and dielectric loss (shown in squares) of BCZT at 100 KHz. The sharp drop of dielectric constant value at 4.7 GPa indicating loss of ferroelectric nature

dielectric loss, at frequency 100 KHz. In this frequency, at 0.35 GPa, the ϵ value is calculated to be 61. As pressure increases, ϵ almost remain constant up to 0.8 GPa, then rapidly rises to 96 at 4.37 GPa pressure, followed by a sharp drop at about 4.7 GPa signifies the loss of the ferroelectric nature of BCZT. Then afterward, it shows a flat nature with almost no change in value.

To understand the direct structural changes, ambient and high-pressure x-ray diffraction studies are performed.

While indexing the XRD patterns at 0.3 GPa, we get a better match with only tetragonal phase. The hkl values have been assigned following Coondoo et al³ and the Rietveld refinement provides us a best-fit that is shown in Figure 1B. If we examine the XRD patterns from 4.8 GPa onwards, we observe that the doublet peaks (broad peaks) in the tetragonal phase (Space Group: P4mm) merge to form a single sharper Bragg reflection. The XRD pattern at 4.8 GPa could only be described by a cubic phase (Pm3m - space group). After Rietveld refinement (shown in Figure 1C), the best-fit gives us the value of lattice parameter, $a = 3.9640(1) \text{ \AA}$ with cell volume = $62.288(3) \text{ \AA}^3$. We have plotted c/a ratio with pressure for tetragonal phase and shown in Figure 6. The value of c/a ratio changes from 1.005 to 1 at 4.8 GPa, indicating a transformation to cubic structure.

However, since the tetragonal and cubic structures are close, we have carried out Rietveld fit of the XRD pattern at 4.8 GPa using the tetragonal model and 0.3 GPa XRD pattern using cubic model. Both the fits are shown in Figure 7, which show a poorer fit due to high value of residuals. This gives us confidence to confirm the structural transitions observed at high pressures.

The system remains in this configuration up to the highest pressure value of our study, 20.5 GPa. After the Rietveld refinement, the unit cell volume obtained from each XRD pattern of different pressure points has been used in the EoSFit program for the BM-EOS fitting.⁴⁶ The volume data as a function of pressure both in the tetragonal and cubic phases are fitted to the third-order Birch-Murnaghan equation of state (BM-EOS) represented by

$$P(V) = \frac{3B_0}{2} \left[\left(\frac{V_0}{V} \right)^{7/3} - \left(\frac{V_0}{V} \right)^{5/3} \right] \times \left\{ 1 + \frac{3}{4} (B' - 4) \left[\left(\frac{V_0}{V} \right)^{2/3} - 1 \right] \right\},$$

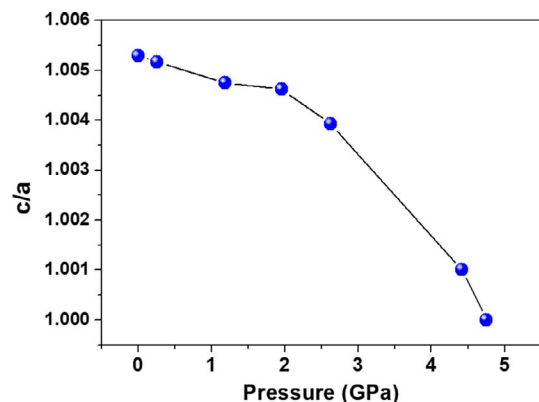


FIGURE 6 The change in the lattice parameter c/a ratio with pressure

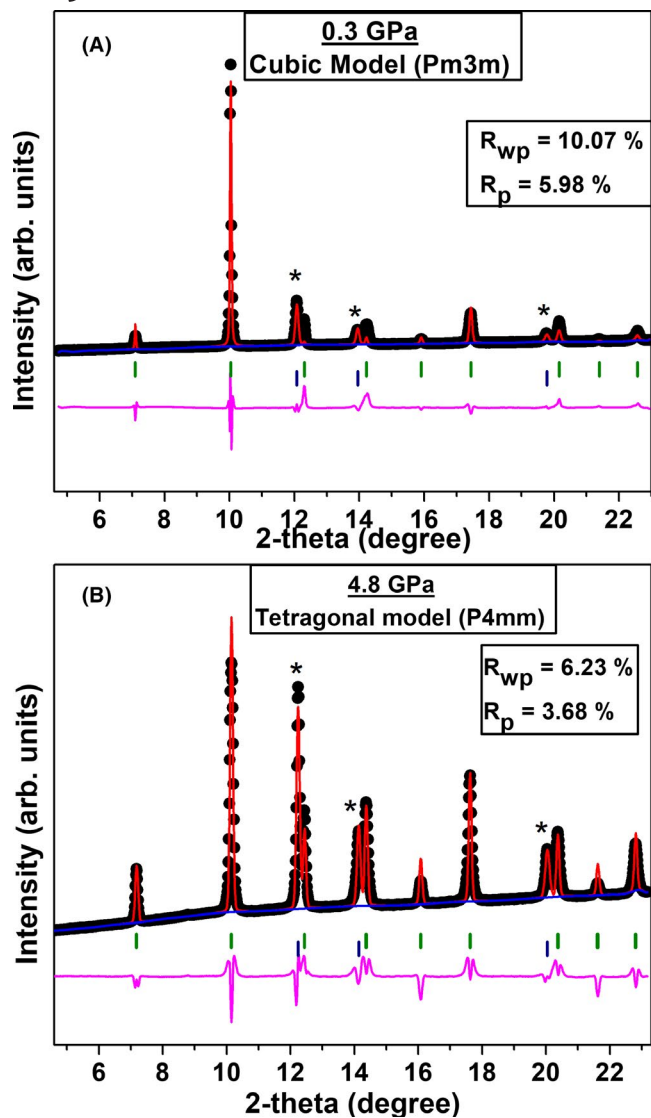


FIGURE 7 A, 0.3 GPa XRD data fitted with cubic model and (B) 4.8 GPa XRD data fitted with tetragonal model show the unsatisfactory result in fitting. This helps understand the need of a correct model for low-pressure and high-pressure range data and confirms the transition taking place at higher pressures. The "*" indicates the pressure marker Ag peaks

where V_0 is the initial volume (in ambient), B_0 is the bulk modulus, and B' is the first pressure derivative of bulk modulus. From the fitting (see Figure 8A,B), we get the best-fit values along with χ^2 -value of fit. The values obtained from the best-fit lines are: (a) for tetragonal phase: $V_0 = 64.3(1) \text{ \AA}^3$, $B_0 = 149(3) \text{ GPa}$; and (b) for cubic phase: $V_0 = 64.2(1) \text{ \AA}^3$, $B_0 = 145(1) \text{ GPa}$. The inverse of the bulk modulus gives us the compressibility. From Figure 8A,B, we can say that although there is a very little difference in the Bulk modulus values in the two phases, still the compressibility in the tetragonal phase is less compared to the Cubic phase. The slight difference in the bulk moduli between the above two

phases signify that other than the effect of pressure on the lattice parameters of the system, some other factor is more responsible for this transition. From Raman Spectroscopy measurements this part can be identified to be the octahedral distortion. To understand this, using the final refinement results, a 3-D polyhedron model of BCZT has been generated for each pressure values using the VESTA software.⁴⁷ Now, we wish to understand how the (Ti/Zr)O₆ octahedra is changing with pressure. The variation of polyhedral volume and the distortion index is shown in Figure 8C. The huge change in the polyhedral volume is clearly implying the tetragonal to cubic phase transition. Whereas in Figure 8D, we observe that the distortion index is increasing very rapidly from ambient to 5.5 GPa, after that it almost reaches to a saturation, then again after 10 GPa, the distortion index starts increasing, but the rate is very low. It can be summed up that with the application of pressure, the (Ti/Zr)O₆ octahedra is getting distorted very rapidly and trying to get into a more symmetric cubic structure, then after reaching there it stabilizes, for that we see the saturation. However, further increase in pressure makes the system a bit unstable, that is why a slight increasing nature of the distortion index after 10 GPa is observed. This slight change in the distortion index beyond 10 GPa might indicate a possible isostructural transition as proposed by Moriwake et al⁴⁸ for the parent BaTiO₃. Appearance of new high-frequency Raman modes (ω_4 and ω_5) also corroborate the above fact. Our high-pressure work on this important piezoelectric material BCZT shows that proper characterization under strained condition is important to predict and understand its electrical properties, which may be useful in future applications.

4 | CONCLUSION

In conclusion, high-pressure Raman spectroscopy, x-ray diffraction, and AC dielectric measurements have been carried out for BaTiO₃-based lead-free piezoelectric sample 0.5Ba(Ti_{0.8}Zr_{0.2})O₃ – 0.5(Ba_{0.7}Ca_{0.3})TiO₃. High-pressure XRD studies have indicated two structural phase transitions. One is at 0.3 GPa, where the system changes from mixed phase to only tetragonal phase. Another one is at about 4.8 GPa, which corresponds to the tetragonal-cubic phase transition. The sudden change in the dielectric constant value at 4.7 GPa, corroborates the aforesaid result. High-pressure Raman spectroscopy results also compliment this finding. Softening of certain Raman modes and line shape changes in the Raman spectra confirms the ferroelectric to paraelectric transition. Slight mismatch in pressure values in between XRD and Raman studies is probably due to the use of two different techniques, where XRD gives an average result in contrast to Raman spectroscopy, which gives microscopic information. The presence of Raman modes even

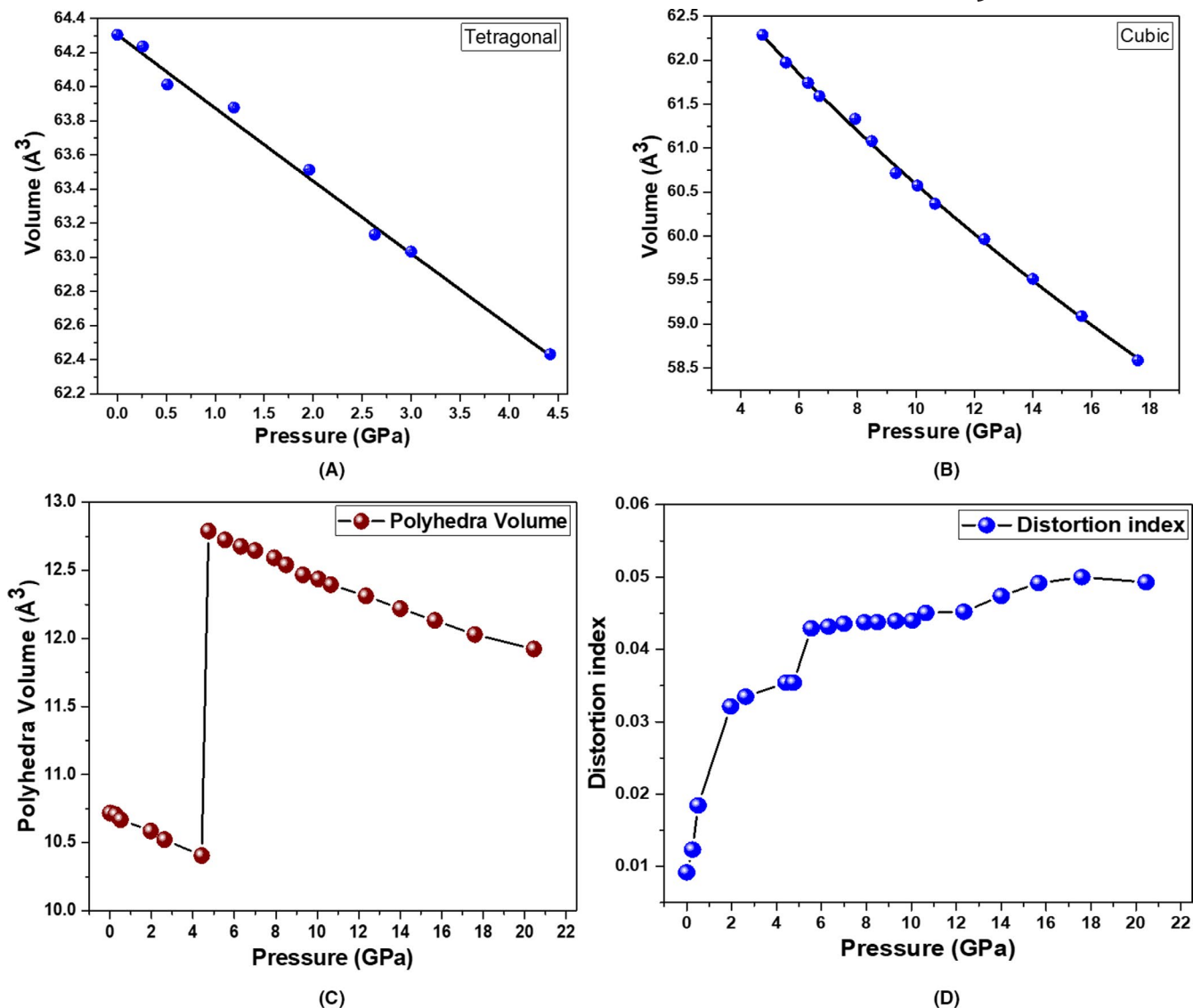


FIGURE 8 Birch-Murnaghan equation of state fit of pressure-volume data of BCZT in (A) tetragonal phase, and (B) cubic phase. (C) Change in polyhedral volume and (D) distortion index of $(\text{Ti/Zr})\text{O}_6$ octahedra in BCZT is shown. A huge change in octahedra volume is seen at the tetragonal to cubic transition at 4.8 GPa. The distortion index (D) gets saturated after reaching the cubic phase but beyond 10 GPa, followed by a slight variation

in the cubic phase is due to the distortion in the $(\text{Ti/Zr})\text{O}_6$ octahedra.

ACKNOWLEDGMENTS

The authors gratefully acknowledge the Ministry of Earth Sciences, Government of India, for the financial support under the grant No. MoES/16/25/10-RDEAS to carry out this high-pressure research work. AM also gratefully acknowledges the fellowship grant from the CSIR program by the Human Resource Development Group, Government of India. The authors also gratefully acknowledge the financial support from the Department of Science and Technology, Government of India to visit XPRESS beamline in the ELETTRA Synchrotron light source under the Indo-Italian Executive Program of Scientific and Technological Cooperation.

ORCID

Goutam Dev Mukherjee  <https://orcid.org/0000-0002-5388-743X>

REFERENCES

1. Cross E. Lead-free at last. *Nature*(London). 2004;432(7013):24–5.
2. Rodel J, Jo W, Seifert KT, Anton EM, Granzow T, Damjanovic D. Perspective on the development of lead-free piezoceramics. *J Am Ceram Soc.* 2009;92(6):1153–77.
3. Coondoo I, Panwar N, Amorín H, Alguero M, Kholkin AL. Synthesis and characterization of lead-free $0.5\text{Ba}(\text{Zr}_{0.2}\text{Ti}_{0.8})\text{O}_3-0.5(\text{Ba}_{0.7}\text{Ca}_{0.3})\text{TiO}_3$ ceramic. *J Appl Phys.* 2013;113(21):214107.
4. Porta M, Lookman T. Effects of tricritical points and morphotropic phase boundaries on the piezoelectric properties of ferroelectrics. *Phys Rev B.* 2011;83(17):174108.

5. Bai Y, Han X, Qiao L. Optimized electrocaloric refrigeration capacity in lead-free $(1-x)\text{BaZr}_{0.2}\text{Ti}_{0.8}\text{O}_3 - x\text{Ba}_{0.7}\text{Ca}_{0.3}\text{TiO}_3$ ceramics. *Appl Phys Lett*. 2013;102(25):252904.
6. Liu W, Ren X. Large piezoelectric effect in Pb-free ceramics. *Phys Rev Lett*. 2009;103(25):257602.
7. Damjanovic D, Biancoli A, Batooli L, Vahabzadeh A, Trodahl J. Elastic, dielectric, and piezoelectric anomalies and raman spectroscopy of $0.5\text{Ba}(\text{Zr}_{0.2}\text{Ti}_{0.8})\text{O}_3-0.5(\text{Ba}_{0.7}\text{Ca}_{0.3})\text{TiO}_3$. *Appl Phys Lett*. 2012;100(19):192907.
8. Keeble DS, Benabdallah F, Thomas PA, Maglione M, Kreisel J. Revised structural phase diagram of $(\text{Ba}_{0.7}\text{Ca}_{0.3}\text{TiO}_3) - (\text{BaZr}_{0.2}\text{Ti}_{0.8}\text{O}_3)$. *Appl Phys Lett*. 2013;102(9):092903.
9. Tian Y, Chao X, Jin L, Wei L, Liang P, Yang Z. Polymorphic structure evolution and large piezoelectric response of lead-free $(\text{Ba}, \text{Ca})(\text{Zr}, \text{Ti})\text{O}_3$ ceramics. *Appl Phys Lett*. 2014;104(11):112901.
10. Zhang L, Zhang M, Wang L, Zhou C, Zhang Z, Yao Y, et al. Phase transitions and the piezoelectricity around morphotropic phase boundary in $\text{Ba}(\text{Zr}_{0.2}\text{Ti}_{0.8})\text{O}_3-x(\text{Ba}_{0.7}\text{Ca}_{0.3})\text{TiO}_3$ lead-free solid solution. *Appl Phys Lett*. 2014;105(16):162908.
11. Acosta M, Novak N, Jo W, Rödel J. Relationship between electromechanical properties and phase diagram in the $\text{Ba}(\text{Zr}_{0.2}\text{Ti}_{0.8})\text{O}_3x(\text{Ba}_{0.7}\text{Ca}_{0.3})\text{TiO}_3$ lead-free piezoceramic. *Acta Mater*. 2014;80:48–55.
12. Kalyani AK, Brajesh K, Senyshyn A, Ranjan R. Orthorhombic-tetragonal phase coexistence and enhanced piezo-response at room temperature in Zr, Sn, and Hf modified BaTiO_3 . *Appl Phys Lett*. 2014;104(25):252906.
13. Gao J, Xue D, Wang Y, Wang D, Zhang L, Wu H, et al. Microstructure basis for strong piezoelectricity in Pb-free $\text{Ba}(\text{Zr}_{0.2}\text{Ti}_{0.8})\text{O}_3x(\text{Ba}_{0.7}\text{Ca}_{0.3})\text{TiO}_3$ ceramics. *Appl Phys Lett*. 2011;99(9):092901.
14. Gao J, Zhang L, Xue D, Kimoto T, Song M, Zhong L, et al. Symmetry determination on Pb-free piezoceramic $0.5\text{Ba}(\text{Zr}_{0.2}\text{Ti}_{0.8})\text{O}_3-0.5(\text{Ba}_{0.7}\text{Ca}_{0.3})\text{TiO}_3$ using convergent beam electron diffraction method. *J Appl Phys*. 2014;115(5):054108.
15. Bjørnnetun Haugen A, Forrester JS, Damjanovic D, Li B, Bowman KJ, Jones JL. Structure and phase transitions in $0.5\text{Ba}(\text{Zr}_{0.2}\text{Ti}_{0.8})\text{O}_3-0.5(\text{Ba}_{0.7}\text{Ca}_{0.3})\text{TiO}_3$ from 100 C to 150 C. *J Appl Phys*. 2013;113(1):014103.
16. Ehmke MC, Khansur NH, Daniels JE, Blendell JE, Bowman KJ. Resolving structural contributions to the electric-field-induced strain in lead-free $(1-x)\text{Ba}(\text{Zr}_{0.2}\text{Ti}_{0.8})\text{O}_3-x(\text{Ba}_{0.7}\text{Ca}_{0.3})\text{TiO}_3$ piezoceramics. *Acta Mater*. 2014;66:340–8.
17. Brajesh K, Abebe M, Ranjan R. Structural transformations in morphotropic-phase-boundary composition of the lead-free piezoelectric system $\text{Ba}(\text{Ti}_{0.8}\text{Zr}_{0.2})\text{O}_3(\text{Ba}_{0.7}\text{Ca}_{0.3})\text{TiO}_3$. *Phys Rev B*. 2016;94(10):104108.
18. Brajesh K, Tanwar K, Abebe M, Ranjan R. Relaxor ferroelectricity and electric-field-driven structural transformation in the giant lead-free piezoelectric $(\text{Ba}, \text{Ca})(\text{Ti}, \text{Zr})\text{O}_3$. *Phys Rev B*. 2015;92(22):224112.
19. Yang T, Ke X, Wang Y. Mechanisms responsible for the large piezoelectricity at the tetragonal-orthorhombic phase boundary of $(1-x)\text{BaZr}_{0.2}\text{Ti}_{0.8}\text{O}_3 - x\text{Ba}_{0.7}\text{Ca}_{0.3}\text{TiO}_3$ system. *Sci Rep*. 2016;6(1):1–8.
20. Fan Z, Zhou C, Ren X, Tan X. Domain disruption and defect accumulation during unipolar electric fatigue in a bzt-bct ceramic. *Appl Phys Lett*. 2017;111(25):252902.
21. Hao J, Bai W, Li W, Zhai J. Correlation between the microstructure and electrical properties in high performance $(\text{Ba}_{0.85}\text{Ca}_{0.15})(\text{Zr}_{0.1}\text{Ti}_{0.9})\text{O}_3$ leadfree piezoelectric ceramics. *Phys Rev B*. 2012;85(6):1998–2006.
22. Piorra A, Petraru A, Kohlstedt H, Wuttig M, Quandt E. Piezoelectric properties of $0.5(\text{Ba}_{0.7}\text{Ca}_{0.3}\text{TiO}_3)0.5[\text{Ba}(\text{Zr}_{0.2}\text{Ti}_{0.8})\text{O}_3]$ ferroelectric lead-free laser deposited thin films. *J Appl Phys*. 2011;109(10):104101.
23. Parjansri P, Intatha U, Eitssayeam S. Dielectric, ferroelectric and piezoelectric properties of Nb⁵⁺ doped BCZT ceramics. *Mater Res*. 2015;65:61–7.
24. Shi J, Lu X, Shao J, Fang B, Zhang S, Du Q, et al. Effects on structure and properties of BCZT lead-free piezoelectric ceramics by rare-earth doping. *Ferroelectrics*. 2017;507(1):186–97.
25. Liu X, Chen Z, Fang B, Ding J, Zhao X, Xu H, et al. Enhancing piezoelectric properties of BCZT ceramics by Sr and Sn co-doping. *J Alloys Compd*. 2015;640:128–33.
26. Li W, Xu Z, Chu R, Fu P, An P. Effect of Ho doping on piezoelectric properties of BCZT ceramics. *Ceram Int*. 2012;38(5):4353–5.
27. Jana R, Pareek V, Khatua P, Saha P, Chandra A, Mukherjee GD. Pressure induced anomalous magnetic behaviour in nanocrystalline YCrO_3 at room temperature. *J Phys Condens Matter*. 2018;30(33):335401.
28. Basu A, Jana R, Mandal G, Chandra A, Mukherjee GD. Pressure driven ferroelectric to paraelectric transition in Sr doped BaTiO_3 . *J Appl Phys*. 2015;117(5):054102.
29. Jana R, Saha P, Pareek V, Basu A, Kapri S, Bhattacharyya S, et al. High pressure experimental studies on CuO : indication of re-entrant multiferroicity at room temperature. *Sci Rep*. 2016;6:31610.
30. Mao HK, Xu JA, Bell PM. Calibration of the ruby pressure gauge to 800 kbar under quasihydrostatic conditions. *J Geophys Res Solid Earth*. 1986;91(B5):4673–6.
31. Dewaele A, Torrent M, Loubeyre P, Mezouar M. Compression curves of transition metals in the Mbar range: experiments and projector augmented-wave calculations. *Phys Rev B*. 2008;78(10):104102.
32. Hammersley AP, Svensson SO, Hanfland M, Fitch AN, Hausermann D. Two-dimensional detector software: from real detector to idealised image or two-theta scan. *High Press Res*. 1996;14(4–6):235–48.
33. Shirley R. The Crysfire 2002 system for automatic powder indexing. Guildford, Surrey, England; 2002. <http://www.ccp14.ac.uk/tutorial/cryst/>.
34. Toby BH. EXPGUI, a graphical user interface for GSAS. *J Appl Cryst*. 2001;34(2):210–3.
35. Achary SN, Mukherjee GD, Tyagi AK, Godwal BK. New polymorph of HfMo_2O_8 synthesized using a high-pressure and high-temperature toroid anvil setup. *Phys Rev B*. 2002;66(18):184106.
36. Venkateswaran UD, Naik VM, Naik R. High-pressure Raman studies of polycrystalline BaTiO_3 . *Phys Rev B*. 1998;58(21):14256.
37. Singh G, Sathe V, Tiwari VS. Investigation of rhombohedral-to-tetragonal phase transition in $0.5\text{Ba}(\text{Ti}_{0.8}\text{Zr}_{0.2})-0.5(\text{Ba}_{0.7}\text{Ca}_{0.3})\text{TiO}_3$ lead-free ferroelectric using micro-Raman scattering. *J Electron Mater*. 2017;46(8):4976–80.
38. Freire JD, Katiyar RS. Lattice dynamics of crystals with tetragonal BaTiO_3 structure. *Phys Rev B*. 1988;37(4):2074.
39. DiDomenico M Jr, Wemple SH, Porto SP, Bauman RP. Raman spectrum of single-domain BaTiO_3 . *Phys Rev*. 1968;174(2):522.
40. Farhi R, El Marssi M, Simon A, Ravez J. A Raman and dielectric study of ferroelectric ceramics. *Eur Phys J B*. 1999;9(4):599–604.
41. Ouni IB, Chapron D, Aroui H, Fontana MD. Ca doping in BaTiO_3 crystal: effect on the Raman spectra and vibrational modes. *J Appl Phys*. 2017;121(11):114102.

42. Mahajan A, Graça MP, Mendiratta SK, Monteiro JM, Valente MA. Structure and ferroelectric studies of $(\text{Ba}_{0.85}\text{Ca}_{0.15})(\text{Ti}_{0.9}\text{Zr}_{0.1})\text{O}_3$ piezoelectric ceramics. *Mater Res*. 2013;48(10):4395–401.
43. Wada S, Suzuki T, Osada M, Kakihana M, Noma T. Change of macroscopic and microscopic symmetry of barium titanate single crystal around curie temperature. *Jpn J Appl Phys*. 1998;37(9S):5385.
44. Sood AK, Chandrabhas N, Muthu DV, Jayaraman A. Phonon interference in BaTiO_3 : high-pressure Raman study. *Phys Rev B*. 1995;51(14):8892.
45. Scarisoreanu ND, Craciun F, Moldovan A, Ion V, Birjega R, Ghica C, et al. High permittivity $(1-x)\text{Ba}(\text{Zr}_{0.2}\text{Ti}_{0.8})\text{O}_3-x(\text{Ba}_{0.7}\text{Ca}_{0.3})\text{TiO}_3$ ($x=0.45$) epitaxial thin films with nanoscale phase fluctuations. *ACS Appl Mater Interfaces*. 2015;7(43):23984–92.
46. Angel RJ, Alvaro M, Gonzalez-Platas J. EosFit7c and a Fortran module (library) for equation of state calculations. *Z Kristallogr Cryst Mater*. 2014;229(5):405–19.
47. Momma K, Izumi F. VESTA 3 for three-dimensional visualization of crystal, volumetric and morphology data. *J Appl Cryst*. 2011;44(6):1272–6.
48. Moriwake H, Koyama Y, Matsunaga K, Hirayama T, Tanaka I. Isostructural phase transitions of tetragonal perovskite titanates under negative hydrostatic pressure. *J Phys Condens Matter*. 2008;20(34):345207.

How to cite this article: Mondal A, Saha P, Ghosh B, et al. High-pressure structural investigation on lead-free piezoelectric $0.5\text{Ba}(\text{Ti}_{0.8}\text{Zr}_{0.2})\text{O}_3 - 0.5(\text{Ba}_{0.7}\text{Ca}_{0.3})\text{TiO}_3$. *J Am Ceram Soc*. 2020;00:1–11. <https://doi.org/10.1111/jace.17167>